AC LOSS IN MGB2-BASED FULLY SUPERCONDUCTING ELECTRIC MACHINES

BY

MATTHEW FEDDERSEN

THESIS

Submitted in partial fulfillment of the requirements
for the degree of Master of Science in Electrical and Computer Engineering
in the Graduate College of the
University of Illinois at Urbana-Champaign, 2017

Urbana, Illinois

Adviser:

Associate Professor Kiruba Sivasubramaniam Haran

ABSTRACT

Superconducting electric machines have shown potential for dramatic increases in specific power for applications such as offshore wind generation, turbo-electric distributed propulsion in aircraft, and ship propulsion. Superconductors exhibit zero loss in dc conditions, though ac current produces considerable loss due to hysteresis, eddy currents, and coupling. For this reason, many present designs for such machines are partially superconducting, meaning that the dc field components are superconducting while the ac armature coils are normal copper conductors. A fully superconducting machine would involve both superconducting field and armature components for higher specific power, though this would introduce the previously mentioned ac losses. This research aims to characterize the expected losses in the components of fully superconducting machines based on partially superconducting designs described in prior work. Various factors are examined, such as motor geometry and operating frequency, and two low-loss designs are proposed based on the analysis.

To my parents, for their love and support.

ACKNOWLEDGMENTS

First and foremost I wish to thank my adviser, Dr. Kiruba Haran, for his insight, guidance, and patience throughout my master's degree studies. Many issues and roadblocks were worked out on the whiteboard in his office, and I would not have been able to finish my thesis without his encouragement and advice. Working in his research group has opened my eyes to the world of electrified aircraft and I am excited to work on the cusp of such a technological shift.

The members of the Haran research group have all been sources of great inspiration, motivation, education, and procrastination - all necessary things in the balance between studies and fun. I would especially like to thank David Loder for teaching and guiding me during the first year of my master's degree, as well as providing a solid foundation for my foray into superconducting machines. I would also like to thank Andy Yoon for bringing me out of my shell and helping to involve me in ECE outreach activities such as IEEE, EOH, and PECI.

I want to sincerely thank all of my friends and staff at Hendrick House, the UIUC Formula Electric team, and my family for their never ending support and stress relief.

Finally, I would like to thank NASA and the Grainger Center for Electric Machinery and Electromechanics for their financial support of my research.

TABLE OF CONTENTS

CHAPTER 1

INTRODUCTION

1.1 Problem Motivation

Over the last 100 years transportation has become increasingly electrified, evidenced by the growing prevalence of hybrid/electric automobiles, trains, and ships in operation today. Environmental and economic considerations are driving this trend towards electrification following advances in energy storage and electromechanical technology. More efficient motors and generators aim to replace gas-burning engines, reducing the emission of nitrous and carbon oxides into the environment. Additionally, decreasing costs for energy storage systems such as lithium-ion batteries push commercial opportunities for electrified transportation into the realm of feasibility, matched by a growing public demand.

While electrified automobiles and trains are seeing mass manufacture in industry, aircraft have remained largely rooted in combustion-based designs. Only recently have industrial aviation groups started to shift towards electrifying aircraft, with projects such as the Boeing SUGAR-volt and the NASA NX-3 [1], [2]. Now more than ever, aircraft are of particular interest for electrification for both environmental and economic reasons. The Intergovernmental Panel on Climate Change (IPCC) estimates that aircraft account for up to 3% of all global emissions, with the possibility of that increasing to 15% in 2050 if action is not taken to further reduce current emissions criteria [3]. In a similar vein, the International Air Transport Association predicts an increase in air passengers from 2.4 billion in 2010 to 16 billion in 2050, and an increase in goods transported by air from 40 million tons to 400 million tons by 2050 [4]. These projected increases call for vast improvements in current aircraft systems to reduce both emissions and jet fuel expenditures, and electrification is a promising avenue to achieve these improvements.

While battery technology is steadily improving, current lithium-ion energy density simply will not be able to compete with that of jet fuel. At only 600 kJ/kg, lithium-ion batteries pale in comparison to jet fuel's 46000 kJ/kg. For this reason, the use of only batteries for energy in an aircraft is not practical. A more feasible solution is to use a type of hybrid system design that utilizes both jet fuel and batteries to efficiently drive electric machines and propellers.

One of the challenges associated with such a design is the manufacture and operation of electric machines with high specific power. To achieve desired performance for commercial aircraft, power levels of up to 50MW may be needed. At the current state of the art of 4-9 kW/kg [5], modern motors cannot reasonably operate at the required aircraft power levels without being extraordinarily heavy. An order-of-magnitude increase in specific power is necessary for integration in electric aircraft.

In order to push the performance and specific power of existing electric machines, radical changes to the machine design must be considered. One technology that shows promise is superconducting (SC) wire implemented in place of the traditional copper windings. Because they have zero electrical resistance under dc conditions, SC wires can operate with extremely large currents and magnetic fields and allow for dramatic increases in power for the same volume and weight. Where a traditional motor may have a peak current density around 10 A/mm2 using copper coils, an SC motor can operate with 100, 500, or even 1000 A/mm2 depending on the operating conditions.

One drawback to the implementation of superconductors in a machine is the necessity for more complex cooling systems and mechanical constraints. Since superconductors can only function under cryogenic conditions, practical applications can be rather difficult to implement. This is especially true for electric machines where rotating forces, oscillating magnetic fields and thermally coupled components all jeopardize the superconducting wires. Several groups have proposed solutions to these issues, with concepts such as vacuum torque tubes and liquid cooling systems having already been implemented in some machines [6].

Another challenge is the prediction and mitigation of ac loss in SC components of the machine. While superconductors exhibit zero electrical resistance under dc conditions, time-varying electrical or magnetic fields will lead to loss in the form of heat within the superconductor. For SC field components in

a synchronous machine, this does not pose too much of a problem since the field is typically produced by dc current. Armature components, however, will be carrying large currents at some frequency while experiencing a rotating magnetic field. This will inevitably lead to loss. If this heat cannot be removed by the machine's cooling system, then the temperature of the superconductor will increase until the wire is no longer superconducting. Models for ac loss have been formulated and tested for various superconductors in existing works, but not to great depth in high-power motor applications or equivalent conditions.

1.2 Problem Definition

Many machines have already been designed or built with partially SC components, where the dc field coils of the machine are made with SC wires while the ac components remain copper. This minor substitution allows for great increase in the magnetic flux density within the airgap, which translates to an increase in the machine's specific power. Conveniently, this design does not suffer from ac loss since the field coils carry dc current and will not experience a changing magnetic field relative to the armature field.

By contrast, there are very few fully SC machine designs, where both the armature and field components are made with SC wire. While the inclusion of an SC armature would theoretically increase the specific power even further than a partial SC machine, the effects of ac loss have been shown to be quite substantial relative to the desired power output. The general consensus over the past decade has been that the state of SC wire technology has not been sufficiently developed for high power ac applications such as electric machines in aircraft. However, other lower-frequency applications may show potential for fully SC designs, such as offshore wind or ship propulsion.

This research aims to analyze the ac losses in a fully SC electric machine that utilizes state-of-the-art wire. A design for a partial SC machine intended for electrified aircraft is used as a starting point for the transition to fully SC, and the results are compared to determine the effectiveness and feasibility of the change. Other machine designs are then examined and a general relationship is established between the geometry, application, speed, and resulting loss.

CHAPTER 2

SUPERCONDUCTORS AND AC LOSS

2.1 Overview of Superconducting Materials and Properties

Superconductors are materials that exhibit unique electric and magnetic properties under specific conditions. The most commonly cited condition to enable superconductivity is temperature; many superconducting materials are described with a critical temperature T_c, below which they become superconducting. However, other factors can affect the superconducting state such as applied magnetic field and mechanical stress in the material. These will be addressed in detail along with an explanation of superconductor loss mechanisms.

2.1.1 Properties of Superconductors

The first main property of superconducting materials is zero electrical resistance to dc current. This was discovered by H. Kamerlingh Onnes in 1911, when he noticed that the resistance of mercury suddenly dropped to zero at 4.2 K [7]. Under most operating conditions this is truly zero electrical resistance, not an approximation to zero. In fact, currents have been observed to flow in superconducting rings without any measurable decay for over a year, and nuclear resonance measurements of the field produced by such currents have established a lower bound of 10^5 years for their characteristic decay time [8]. This phenomenon only applies for dc conditions such as constant current and external magnetic field. If the field or current experiences a change over time, heat will be produced in the superconductor due to various loss mechanisms.

The second major property is called the Meissner effect, which describes

the ability of a superconductor to act as a perfect diamagnetic material. As such, an external magnetic field applied to a superconductor will be perfectly opposed by induced currents, preventing any of the magnetic field from entering the material. Additionally, any magnetic field that was penetrating the material while in a normally conductive state would be expelled when the material transitions into a superconducting state. However, this expulsion of magnetic field only applies for fields that are relatively weak.

2.1.2 Conditions for Superconductivity

The first property that is typically used to describe superconductors is the critical temperature, T_c, where a material will transition between the superconducting and normally conducting states. The first discovered superconductors had T_c values below 10 K, though today there are materials that can be considered superconducting at temperatures as high as 130 K [9]. Modern superconductors can be grouped into one of two categories relating to their operating temperature: Low temperature superconductors (LTS) and high temperature superconductors (HTS). LTS have relatively low T_c, typically below 15 K, while HTS have higher T_c values around 77 K or above.

At a given temperature $T < T_c$, if an external magnetic field H is gradually applied, the superconductor will remain stable up until a critical field H_c is reached. At that point the material will become normally conducting. Much as there are two categories of superconductors based on their T_c, there are also two categories based on their magnetic properties. Fig. 2.1a shows the B-H curve of a Type I superconductor,[1] where the superconductor exhibits the Meissner state perfectly until H_c is reached. At that point, all of the external field that was being expelled from the material is able to penetrate. In a Type II superconductor, shown in Fig. 2.1b, the external field penetrates slightly into the material after a 'lower critical field' H_{c1} is reached. The field penetrates gradually further into the material until reaching the 'upper critical field' $H_{c2} = H_c$, at which point the material is no longer superconducting.

[1] B is conventionally considered to be the magnetic field density within the superconducting material while H is the external applied field. This convention will be adhered to during this section's microscopic explanation of superconductors, but later in the thesis the terms for internal and external field will be used interchangeably as B or H.

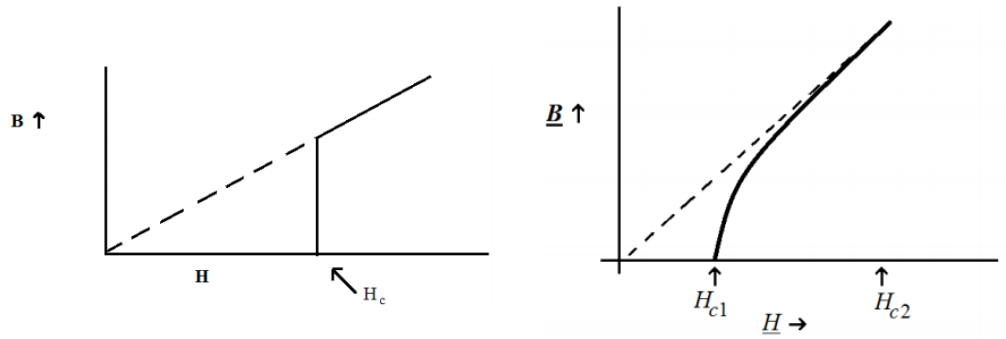

(a) Type I, with no penetrated field before H_c

(b) Type II, showing partial penetration beginning after H_{c1}

Figure 2.1: Comparison of magnetic behavior of Type I and II materials [10]

Another factor that affects superconductivity is the amount of current flowing through the superconducting material. This current, called transport current, can cause the material to lose its superconducting properties if it passes a critical current value I_c. This is particularly undesirable in superconducting applications carrying large current, since the sudden transition to the normal state will create huge ohmic losses with the re-introduction of electrical resistance, potentially burning up the system. This energetic failure mode is known as 'quench'.

Finally, mechanical strain can affect the superconducting state. This is specific to shaped superconductor components that are expected to experience mechanical stresses, such as wires in a large magnetic coil. While critical temperature, field, and current are commonly measured and provided for various superconductors, critical strain limits are not as readily available. However, some general engineering guidelines exist for many common designs. For instance, ITER magnet design criteria specify the maximum permissible tensile strain of Nb_3Sn as 0.2 %, which is feasible for most applications [11].

Together these four parameters (temperature, external magnetic field, transport current, and strain) form what is known as the critical surface, under which a material will be in the superconducting state [12]. In other words, at any particular temperature value $T < T_c$ the critical values of magnetic field, transport current, and mechanical strain can be charted as a 3-dimensional curved surface, much like in Fig. 2.2. If any of the operating parameters venture out of this surface, the material will become normally conducting. Note how the critical surface shrinks with increasing temperature. For this

reason, many superconductors are utilized at temperatures far below their T_c, to maximize their operating range based on the critical surface.

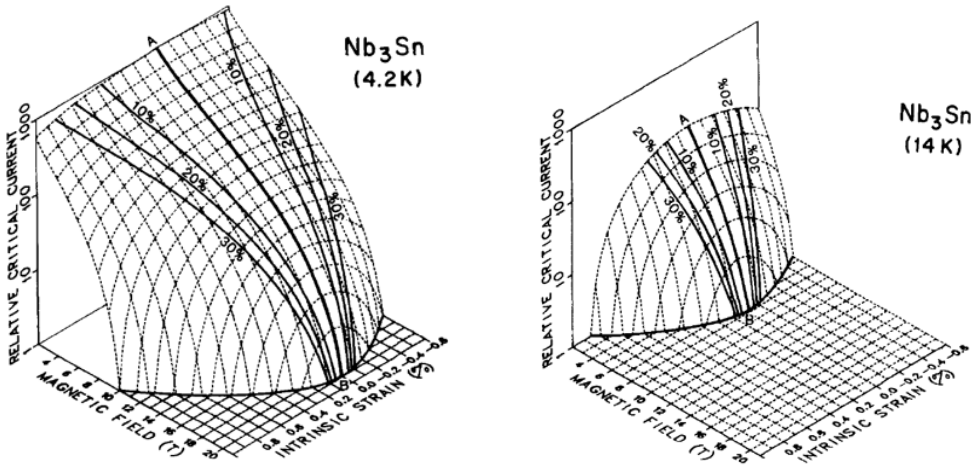

(a) (b)

Figure 2.2: Critical surface comparison of Nb_3Sn at (a) 4 K and (b) 14 K [12]

2.1.3 Common Superconducting Materials

Common superconducting materials and their main distinguishing properties are shown in Table 2.1. The most commonly used material in modern applications is niobium-titanium (NbTi), which is known for being used as the primary magnetic field coils in the experimental fusion device, Wendelstein 7-X. Next is niobium-tin (Nb_3Sn), which has a higher critical temperature and can withstand larger magnetic fields than NbTi. However, it is more expensive and still can only be used practically at 4.2 K. Magnetic field coils in the ITER nuclear fusion tokamak project are currently being constructed with Nb_3Sn. Both NbTi and Nb_3Sn are considered to be LTS materials since they are typically operated around 4 K.

HTS materials include YBCO and BSCCO, since both of these materials can operate at the relatively high temperature of 77 K while still remaining superconducting. YBCO stands for yttrium-barium-copper-oxide, and is famous for being the first superconductor that was discovered to have a critical temperature above 77 K.

Table 2.1: Common superconducting materials and wires

Name	Critical Temp (K)	Typical Operating Temp (K)	Wire type
NbTi	9	4.2	multifilament
Nb_3Sn	18	4.2	multifilament
MgB_2	39	20	multifilament or tape
YBCO	90	77	tape
BSCCO	108	30-35	tape

The LTS and HTS temperatures, 4 K and 77 K respectively, are chosen based on the bath immersion liquid cooling that can be utilized for each type. Liquid helium, which boils at 4.2 K, can be used to reliably cool LTS materials while liquid nitrogen can cool HTS materials due to its 77 K boiling point. Between HTS and LTS materials, MgB_2 occupies the role of a possible 'medium temperature superconductor' since its transition temperature of 39 K allows potential cooling through liquid hydrogen, which boils at 20 K. For desired operating points that vary from the established liquid boiling points, closed cycle cryogen refrigeration or conduction cooling can be utilized, such as for typical BSCCO applications. Additionally, superconductors with higher transition temperatures are being sought after for the possibility of cooling with liquid natural gas (boiling at 110 K).

2.2 Analytical Models

While superconductors exhibit zero resistance (and thus no power loss) under dc conditions, changes in transport current or magnetic field will result in loss and create heat. In pure superconducting materials most of this loss is considered to be a form of hysteresis, since the loss is nonlinear, cyclical, and generally independent of the ac cycle length. This loss can be modelled in both a macroscopic and a microscopic sense.

Macroscopically, a changing magnetic field induces an emf in the superconductor that can drive induced currents beyond the critical I_c value and into a non-superconducting region. Thus the power loss per unit volume is simply $p = E \cdot J$, and a total power loss can be calculated by integrating p over the entire region.

Microscopically, ac losses can be visualized as the viscous motion of quantized units of magnetization, which form when the superconductor carries transport current or magnetic field about H_{c1}. These discrete units of magnetization are called fluxons, fluxoids, or Abrikosov vortices in the literature. As the transport current or magnetic field periodically changes, a Lorentz force is exerted on these fluxons in an effort to reorient them, causing them to oscillate and dissipate energy.

Both the macroscopic and microscopic models have been verified experimentally, but the macroscopic view is typically easiest to implement in calculations and loss predictions. From this macroscopic theory and experimental observations, two common models have been established for analytical evaluations of superconductor loss: the critical state model and the power law.

2.2.1 Critical State Model

The exact interaction between fluxons and the Lorentz force, or the exact distribution of E and J in the superconductors, can be difficult to precisely model. For practical purposes an approximation known as the critical state model (CSM) can be utilized for fairly accurate predictions regarding the macroscopic behavior of the superconducting material.

The CSM assumes that at any point in time, the total current I in a superconductor can be expressed as a combination of current densities J_c and 0 in various regions of the cross section [13]. Due to the Meissner effect, these current-carrying regions will initially crowd around the 'skin' of the superconductor for low values of I, but as the total current increases the size of the current-carrying regions will increase to compensate. If the wire is carrying only 60% of its critical current value, then 60% of the wire cross section would be occupied by J_c.

For dc current, there are only regions of either critical current density or zero current density in the wire cross section, but for alternating current or magnetic field a region of negative current can be introduced. This mechanism is illustrated in Fig. 2.3, where the total current in the conductor is the sum of $+J_c$, $-J_c$, and 0 regions depending on what portion of the ac cycle is being measured. As current increases, more of the wire cross section is occupied by positive J_c, but as current decreases then that region is replaced

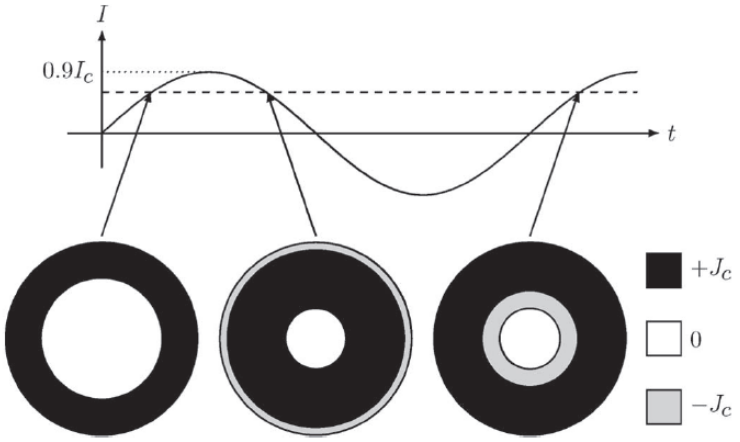

Figure 2.3: Current density distribution in the cross section of a circular SC wire, measured at different instants for the same instantaneous current value [14]

with negative J_c.

Most analytical equations relating superconductor parameters with ac loss are formulated with the CSM. Even with this simplified model, loss equations tend to be quite complex. For computer simulations and finite element models, the power law is more commonly employed.

2.2.2 Power Law

While the CSM is a useful approximation for bulk superconductors (pure superconducting material) experiencing low magnitudes of current and magnetic field, it is insufficient for situations near the critical boundary. Additionally, it does not account for the fact that the transition between superconducting and non-superconducting states can be very gradual across the operating temperature range, leading to effective loss.

To account for these deficiencies, a formulation known as the 'power law' can be used to relate the current density and the electric field, written in Eq. 2.1. Of note is the characteristic electric field value E_c, which sets a measurable value on the definition of superconductivity; that is, if J rises to the point where E is measured[2] as E_c, then the material is no longer considered superconducting, and that J value is then established to be the

[2] E_c is usually standardized as 10^{-4} V/m for all applications.

critical J_c value of the material under its current operating conditions.

$$J = J_c(\frac{E}{E_c})^{\frac{1}{n}} \tag{2.1}$$

Another notable parameter in the power law is the n-value. This represents the steepness of the material's transition between superconducting and non-superconducting states, or the slope of the E-J curve. Higher values of n (above 50) approach the behavior of the CSM. Most practical superconductors exhibit n-values below 50, however. An n-value of 1 would be a purely resistive material.

For a given point in the superconductor, Maxwell's equations can be utilized to calculate either J or E, and the power law (Eq. 2.1) can then be used to calculate the corresponding E or J. The power loss $p = E \cdot J$ can be calculated and the procedure repeated across the entire region to compute total loss.

2.3 AC Loss

From the CSM, various expressions for loss have been determined for pure superconducting materials. Most of these losses are due to changes in magnetic field, current, or both, and are labelled as hysteresis due to their frequency-independent behavior and their basis in magnetization energy theory.

2.3.1 Loss Due to Changing Magnetic Field

In the case of a changing magnetic field transverse to a section of Type II bulk superconductor,[3] the material will produce circular screening currents that completely expel the magnetic field. This is the aforementioned Meissner effect, and is valid for low values of B. From the CSM, these screening currents will occupy a finite region in the material's cross section, as shown in Fig. 2.4. As the magnitude of B increases, it will start to penetrate the material and more screening currents will be generated in an effort to expel it. These screening currents will create a magnetization M in the

[3]All superconductors of interest in high-field applications are Type II, so these will be the referenced superconductor type in this thesis.

material, which will increase with the amount of screening current. At a certain magnitude of magnetic field, B_p, the entire cross section is occupied by screening currents as the B field has managed to penetrate to the center of the material. The applied B field can continue to increase beyond B_p, but the screening currents will not increase to compensate and thus no further magnetization within the superconductor will occur.

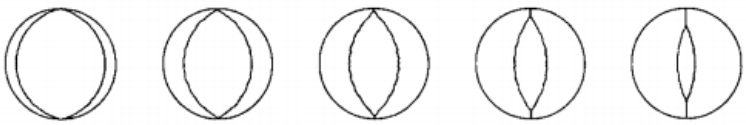

Figure 2.4: Increased screening current area with increased applied H field, left to right [15]

As the applied B field changes, the screening currents will change to compensate. Areas that were previously magnetized will require energy to reorient their magnetization based on the new screening currents, and this energy will come out as heat loss. This is the mechanism for hysteresis loss due to changing magnetic fields.

The penetration field limit B_p is a property of the superconductor, and can be calculated for a circular cross section of material as

$$B_p = \frac{4\mu_0 J_c a}{\pi} \tag{2.2}$$

Formally, the loss in a section of superconductor can be expressed as

$$Q = \int H dM = \int M dH \tag{2.3}$$

where H is the applied magnetic field and M is the magnetization. H is related to B through the constant of magnetic permeability μ_0, such that $B = \mu_0 H$.

The magnitudes of H and M vary based on the geometry of the superconducting cross section, the peak magnetization energy determined by the superconductor properties, and the applied field. The loss described by Eq. 2.3 can be visualized as the area of the hysteresis loop of M versus H, pictured in Fig. 2.5.

Since the height of the hysteresis loop does not change for values greater than B_p, loss formulas were determined from this geometric interpretation,

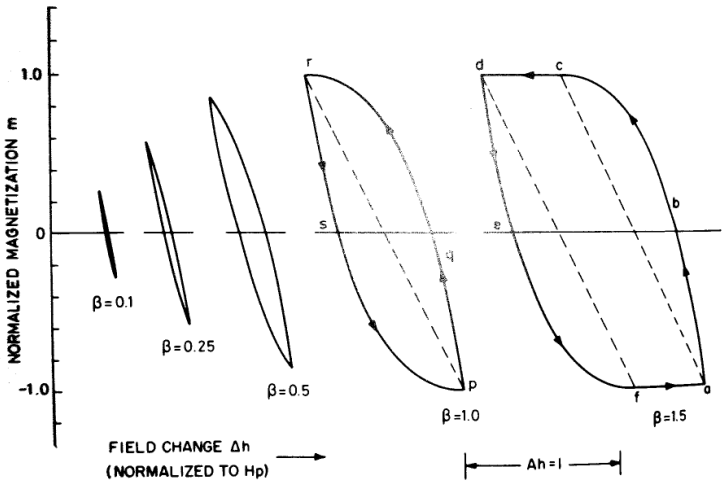

Figure 2.5: Normalized M-H magnetization curve for various amplitudes β of normalized field change [16]

shown as

$$\beta = \frac{B_m}{B_p} \tag{2.4}$$

$$Q_h = \frac{B_m^2}{2\mu_0}\left(\frac{4}{3\beta} - \frac{0.710}{\beta^2}\right), \quad \beta > 1 \tag{2.5}$$

$$Q_h = \frac{B_m^2}{2\mu_0}\frac{4}{3\beta}, \qquad \beta \gg 1 \tag{2.6}$$

where B_m is the peak-to-peak variation of the applied magnetic field. Eq. 2.5 is valid for $\beta > 1$, Eq. 2.6 is a useful approximation for $\beta \gg 1$, and situations with $\beta < 1$ require more numerically complex computations. For simplicity across a wide range of β values, Wilson [16] developed a loss function $\Gamma(\beta)$ to capture the dependence of hysteresis loss on the applied field strength, and thus simplified the hysteresis loss equations to

$$Q_h = \frac{B_m^2}{2\mu_0}\Gamma(\beta) \tag{2.7}$$

$\Gamma(\beta)$ is not representable as a simple engineering equation, since it is based on an integration of the magnetization energy in the hysteresis loop across various states of penetration. Regardless, it serves as a useful simplification and reference when calculating hysteresis loss. A graph of $\Gamma(\beta)$ is shown in

Fig. 2.6 for various wire geometries and field orientations.

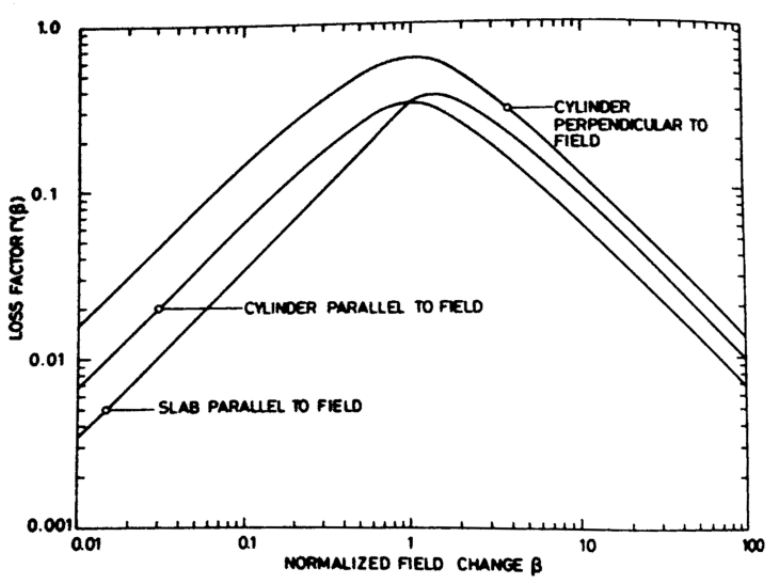

Figure 2.6: Hysteresis loss factor for various amplitudes β of normalized field change [16]

2.3.2 Loss Due to Changing Current

For a superconductor carrying a current with no externally changing magnetic field, CSM predicts that the current will occupy a section of the superconductor relative to the current magnitude and the critical current of the superconductor. The current will occupy sections starting from the outer skin of the superconductor, and then as more current flows through the wire more cross sectional area will be occupied by the current density J_c. When the entire section of wire is carrying current, the critical current has been reached.

Currents flowing through the superconductor produce small magnetic moments not unlike the behavior described in the previous section. As currents change they push against these magnetic moments and expend energy in re-aligning them. Again, this loss is hysteretic.

Norris described the hysteretic loss resulting from ac transport current as a function of the amount of transport current relative to the critical value [17].

$$Q_h = \frac{I_c^2 \mu_0}{\pi}\Big((1-i)\ln(1-i) + i - \frac{i^2}{2}\Big) \tag{2.8}$$

where $i = I_t/I_c$.

This equation has been verified and validated numerous times in the literature, and continues to see use as a first-order predictor for ac loss due to transport current.

2.3.3 Loss Due to Simultaneous Field and Current

Hysteresis loss from both field and current is complicated to analyze, but can be simplified if either the current or field is at a low value. Carr showed that for low currents, the loss can be calculated for the ac field case and then multiplied by a factor based on the critical current fraction. Similarly, for low magnetic fields, the loss can be calculated for the ac current case and then multiplied by a factor based on the penetration field fraction.

In Fig. 2.7 this multiplier is shown for both the ac current and ac field cases. As shown in the upper chart of the figure, large values of applied field converge to a small multiplier regardless of the current, which is verified in experimental data from [19]. For an electric machine application the external field will be fairly large while the current will remain relatively small, so the ac field hysteresis equation coupled with a multiplication factor based on the current would be sufficient for this study. This is shown in Eq. 2.9 with the multiplication factor represented as $\frac{Q(H_0,I_0)}{Q(0,I_0)}$

$$Q_h = \frac{B_m^2}{2\mu_0}\Gamma(\beta)\frac{Q(H_0,I_0)}{Q(0,I_0)} \tag{2.9}$$

Numerical and experimental studies on the effect of phase angle between magnetic field and transport current on superconducting tapes have shown that for low fields and currents, the phase between the two can reduce the hysteretic loss with a minimum at 90°. However, since these studies were performed at low field and currents, they are not entirely proven for higher field applications such as motors. As a result, this phase angle dependence is not considered in this study.

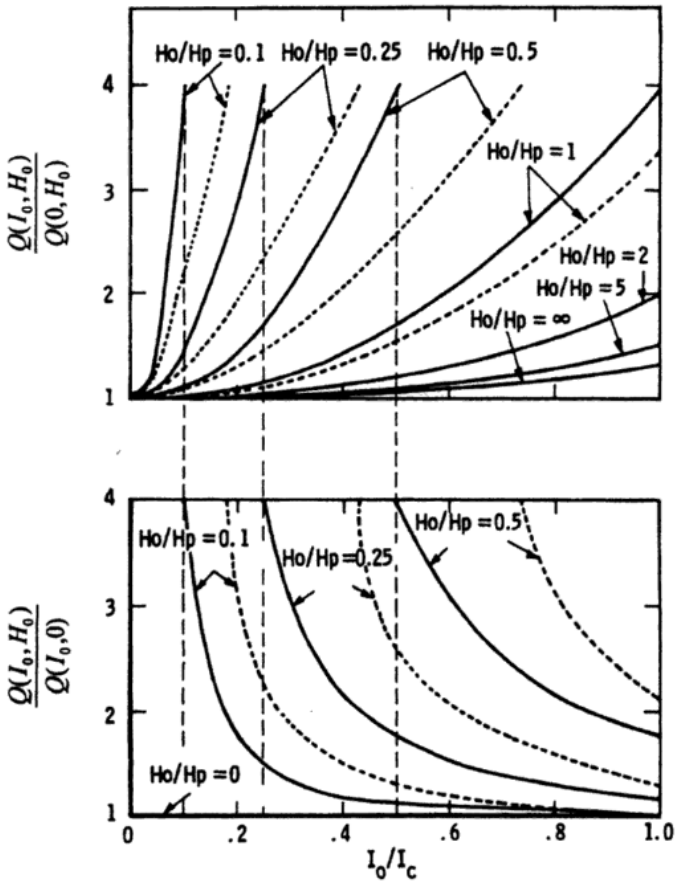

Figure 2.7: Loss multipliers for simultaneous current and field [18]

2.3.4 Multifilamentary Wire Loss

While the hysteretic loss models above have been validated for various field and current parameters, they are not sufficient to describe the ac loss in a practical superconducting wire. In real-world superconductor applications, wire is constructed as a combination of superconducting filaments and a resistive metal matrix. Fig. 2.8 shows an example wire cross section with the darker superconducting filaments situated in a copper matrix. Typically these wires have a twist pitch to reduce proximity currents, also called coupling currents, in a manner that is similar to Litz wire.

Figure 2.8: An example wire cross section, showing darker MgB_2 filaments embedded in a copper matrix [20]

The coupling currents can travel across the resistive matrix between superconducting filaments as a result of changing field, and can dissipate heat through I^2R losses. In this manner the entire wire can be considered to have some effective transverse resistivity ρ_t across it, which is a function of the fraction of superconductor in the cross section of the wire λ, and the resistivity of the matrix ρ.

$$\rho_t = \rho\frac{1+\lambda}{1-\lambda} \tag{2.10}$$

Eq. 2.10 assumes that the wires are fabricated with a heat-treatment process that forms resistive inter-metallic layers between the superconducting filaments and the matrix. If this is not the case, then the numerator and denominator are switched.

The nature of the coupling currents can be encapsulated in an inductive time constant τ within the wire, expressed as

$$\tau = \frac{\mu_0}{2\rho_t}\left(\frac{L}{2\pi}\right)^2 \tag{2.11}$$

where L is the twist pitch of the wire. For a changing external magnetic field $B_e = \frac{1}{2}B_m e^{j\omega t}$, the loss per cycle due to coupling currents is

$$Q_c = \frac{B_m^2}{2\mu_0}\frac{\pi\omega\tau}{(\omega^2\tau^2+1)} \tag{2.12}$$

One notable effect of multifilamentary wires is that the coupling and screening currents in the outermost filaments can reduce the internal magnetic field experienced by the innermost filaments in the wire. This reduces the effective flux linkage within the wire by a factor α, which changes the time constant to $\tau_\alpha = \alpha\tau$. The resulting changes to the hysteresis loss and coupling loss are shown below, modified from Eq. 2.9 and Eq. 2.12 to account for the change due to internal field screening.

$$Q_h = \frac{B_m^2}{2\mu_0}\frac{\lambda}{\omega^2\tau_\alpha^2+1}\Gamma\left(\frac{\beta}{(\omega^2\tau_\alpha^2+1)^{\frac{1}{2}}}\right)\frac{Q(H_0,I_0)}{Q(0,I_0)} \tag{2.13}$$

$$Q_c = \frac{B_m^2}{2\mu_0}\frac{\alpha\pi\omega\tau_\alpha}{(\omega^2\tau_\alpha^2+1)} \tag{2.14}$$

These equations give the hysteresis loss and coupling loss of a round multifilamentary superconducting wire subject to changing magnetic field and current. It is important to note that Q_h and Q_c are in joules per cycle per cubic meter. To convert to power loss in watts for a length of wire, Q must be multiplied by the frequency, the length of wire, and the cross sectional area of the relevant region. For hysteresis loss, the relevant region is only the superconducting section since that is the component that produces hysteretic ac loss. For coupling loss, the relevant region is the entire wire cross section, including both superconductor and matrix area.

CHAPTER 3

FULLY SUPERCONDUCTING MACHINE STUDY

3.1 Actively Shielded Machine Design

3.1.1 Motivation

Multiple SC machines have been designed and reported for various applications, including flux-trapping bulk SC field coils, homopolar motors, axial flux machines, and more traditional wound-field synchronous topologies [21], [22], [23]. Almost all of these designs are partially SC, meaning that some of the electrical components are superconducting while the rest are traditional copper.

Most partially SC machines replace the copper field coils or permanent magnets with superconducting coils carrying dc current. The high current limits of SC wires allow for much stronger magnetic fields, in some cases as high as 10 T [24]. Compared to a machine with traditional copper or permanent magnet field components, a partially SC machine will have a much higher magnetic loading and thus a much higher power density. A general equation to describe the power produced by an electric machine is shown in 3.1, where k is a constant based on the design and units, A is the electrical loading or the linear current density contributing to torque, B is the magnetic loading or magnetic flux density contributing to torque, n is the angular speed, D_{ag} is the air-gap diameter in meters, and L is the active length in meters.

$$P = kABnD_{ag}^2L \tag{3.1}$$

Increasing the electric loading, magnetic loading, diameter, speed, or active length of the machine will increase the power. To achieve high specific power,

the non-geometric parameters (A, B, n) would need to increase, and this is the primary motivation behind using superconductors as they can drastically increase both A and B.

3.1.2 Design

In [24], a design for a partially SC electric machine is proposed with four unique features. First, all flux-carrying core iron in the machine is removed, effectively making this an air-core design. Second, the dc field coils are constructed with Nb_3Sn SC wires, enabling magnetic fields up to 10T to be created. Third, to simplify cooling and rotating stresses on the SC wire, the dc field coils are placed on the outside of the machine and are held stationary while the copper three-phase armature is rotating on the inside of the machine. Finally, to reduce the levels of magnetic field outside the machine an additional set of SC coils is placed on the outer circumference, which actively counteracts the magnetic field outside the machine while leaving the fields in the air gap unaffected. To encompass these design features, the machine is classified as an 'Actively Shielded Air Core Partially Superconducting Synchronous Machine'.

In Fig. 3.1, a cross section of one of the poles in the machine is shown with the armature and field components labelled. The copper armature bars are part of the rotor, and the SC field coils are part of the stator. The compensating SC field coils can be seen just outside the radius of the main SC field coils. For this design, a multi-objective optimization was performed to determine the dimensions, current, and placement of the field coils to maximize the air gap flux while minimizing the external magnetic field.

The partially SC machine design described above serves as a useful starting point for a fully SC design, as the only change would be to set the armature material to be superconducting wire. Additionally, minimal changes to the design allow for a straightforward performance comparison between the partial and full SC designs.

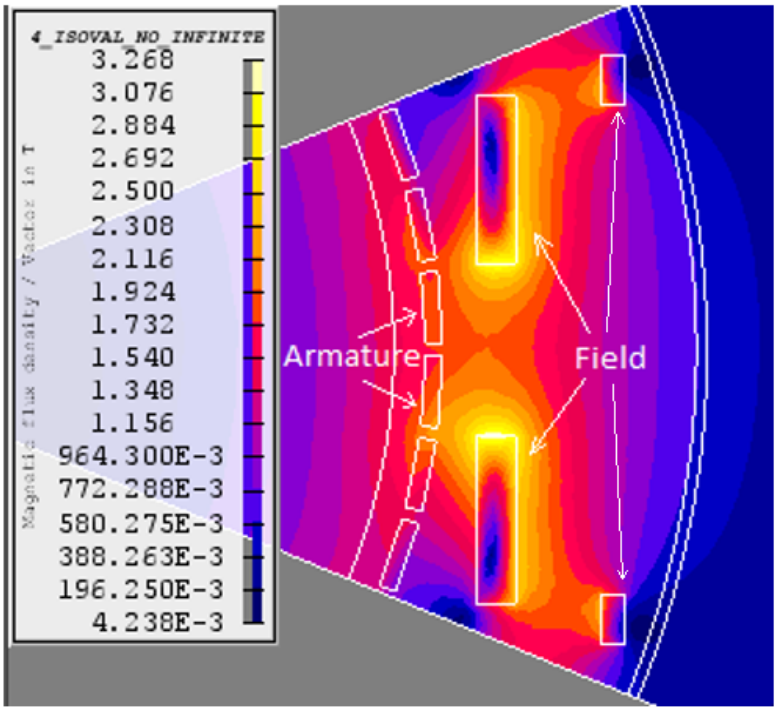

Figure 3.1: Cross section of a single pole of the acitvely shielded air core design, showing the armature and field components.

3.2 Machine Model Setup

3.2.1 Wire Selection

In the transition from the partially SC to fully SC design, some of the operating parameters will need to change. For instance, it is infeasible to operate superconductors in ac conditions at extremely low temperatures (below 15 K) due to the high specific power of cryogenic systems. In other words, the amount of power needed to operate a cryogenic cooling system for a low temperature application increases inversely with temperature. As a baseline reference, 1 W of heat load at 4 K requires upwards of 1000 W of cryogenic power to cool, 1 W of heat load at 20 K requires around 100 W of cryogenic power, and 1 W at 77 K requires around 10 W of cryogenic power [25]. These amounts can change based on the cryocooler and the operating conditions, but they are convenient baselines for initial designs.

Since superconductor properties degrade with increased temperature, a compromise between performance and cryogenic power must be made. The wire for the partial SC design, Nb_3Sn, has a critical temperature around 18 K,

and it is typically operated at 4 K to fully utilize its performance capabilities. Due to the high specific power for cooling at such low temperatures, Nb_3Sn is unusable for an ac application, even if the wire exhibits extremely low ac loss. For these reasons, MgB_2 was chosen as the superconductor material, operating at 20 K.

Other options exist for superconductor materials such as YBCO and BSCCO, which can both operate in the range of 20-77K. While these are lucrative choices based on their high operating temperature, the geometry of these superconductors (tapes instead of circular wires) severely complicates ac loss analysis, and studies have shown that the filament coupling and matrix properties in current YBCO and BSCCO tapes already result in prohibitively large ac losses compared to MgB_2 [26].

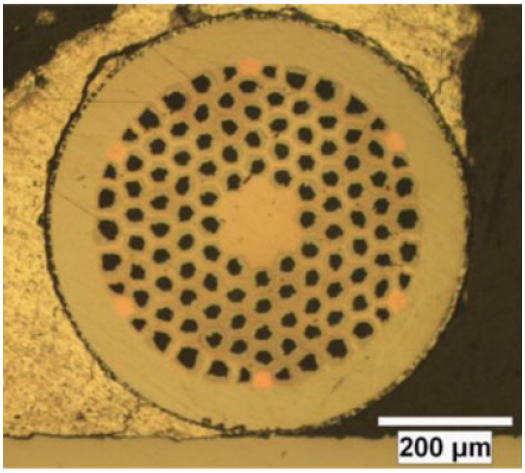

Figure 3.2: Cross sectional area of the MgB_2 wire that was analyzed in this study [27].

The main parameters of the chosen MgB_2 wire are noted in Table 3.1, and a cross-section of the wire is shown in Fig. 3.2. This wire was chosen based on recent work towards the manufacture of multifilamentary MgB_2 wires with low ac loss [27]. As discussed in Chapter 2, hysteresis and coupling losses depend on the geometric and physical properties of the superconducting wire. Improvements such as high critical current density J_c, high matrix resistivity ρ, small filament diameter a, and small twist pitch L will all reduce the ac loss.

The chosen wire was described with data relating the critical current J_c to the applied B field at an operating temperature of 4.2 K only. For the

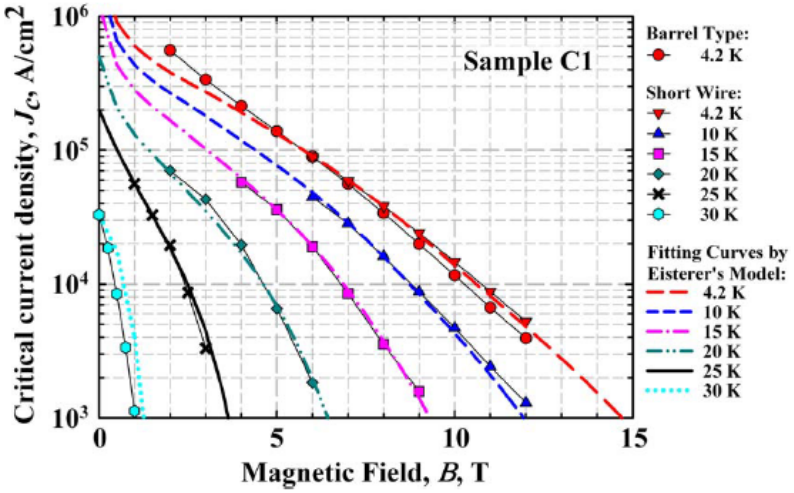

Figure 3.3: Experimental measurements of J_c at various B values for another MgB_2 wire. The J_c curve shown at 4.2 K is very similar to the wire in our study.

behavior of the wire at the desired operating point of 20 K, data from a related paper was utilized, showing the dependence of the $J_c - B$ curve on temperature (Fig. 3.3)[28]. The assumption was made that the J_c values from [28] would degrade with temperature similar to [27]. Since significant work was performed in [27] to show that the overall J_c behavior did not degrade despite various ac loss mitigation changes, we believe that this is a safe assumption.

Table 3.1: MgB_2 wire parameters

Symbol	Parameter	Quantity
J_c	Critical current density at self-field, 20K	2.8e9 A/m2
B_0	Kim-Anderson fitting parameter	0.2
D	Wire diameter	600 mm
a	Filament diameter	20 μm
n	Number of filaments	114
λ	SC fill factor	0.13
L	Twist pitch	5 mm
ρ	Matrix resistivity	23e-8 Ω-m
B_p	Penetration field for a filament	0.35 T

For practical uses of superconductors, the dependence of J_c on B is fairly important since it will determine the operating limits of the wire. In general,

J_c decreases as B increases. The exact relationship between J_c and B can be complicated, but experimental and analytical models help simplify the phenomenon for calculations. One example is the Anderson-Kim model, which is stated in Eq. 3.2. The B_0 parameter in this model is a fitting constant based on experimental data, and for the particular wire that was used in this study B_0 was determined to be 0.2. This gives a slight under-approximation of the $J_c(B)$ dependence, yet is still reasonable for the range of B=0-3 T.

$$J_c(B) = J_c(0)\frac{1}{1+\frac{B}{B_0}} \tag{3.2}$$

The matrix material is a Cu-Ni alloy, and the resistivity was determined from cryogenic resistance data for Cu-Ni alloys of various compositions [29]. Since the exact composition was not mentioned for this wire, 30% Cu was assumed.

3.2.2 Machine Parameters

While the partially SC machine design is being used as a reference, some operating parameters will inevitably change as a result of the different wire and temperature. The first is the critical current density of the field coils. Nb_3Sn had a very large critical current at 4 K, with an operating point of approximately 600 A/mm2. At 20 K, our selected MgB_2 wire was determined to operate safely at 200 A/mm2 in the field coils. These operating points are set to be below the critical current densities of the wires to allow for a margin of safety.

The current density in the armature was set to be 100 A/mm2 (peak) for the fully SC design, up from 10 A/mm2 (peak) in the copper armature design. While this allows us to conservatively increase the electrical loading relative to our wire capabilities, we found that higher values of current in the armature tend to dominate and distort the air-gap B field distribution. For this reason, 100 A/mm2 was set as the operating current density in the armature.

Finally, the peak B field in the field and armature components was chosen and adhered to. A peak value of 3 T still allowed for a large current density in the field coils, and due to the large air gap this also restricted the B field

on the armature to be below 3 T. In simulations the B field did not increase beyond 2.5 T in the armature, though variations on the air gap could vary that.

Table 3.2: Parameter differences between partially and fully SC studies

Symbol	Parameter	Partial SC	Fully SC
	Superconductor	Nb_3Sn	MgB_2
T_{op}	Operating Temperature	4.2K	20K
I_m	Main coil current, dc	906 kA-t	300 kA-t
I_c	Compensating coil current, dc	207 kA-t	60 kA-t
J_a	Armature current density, ac	10 A/mm2	100 A/mm2
B_{dc}	Peak B field in field coils	9 T	3 T
B_a	Peak B field in armature	5 T	0.5-2.5 T

3.3 AC Loss Model

3.3.1 Model Assumptions

A finite element model (FEM) was constructed based on the partial SC machine geometry using the FEM software Magsoft FLUX2D. By solving Maxwell's equations for discrete subsections of the machine geometry, the electromagnetic behavior of the machine can be determined. To simplify the loss models and calculations, and to enable the finite element software to compute parameters without requiring knowledge about superconducting physics, a few initial assumptions were made.

First, since the armature cross section in a fully SC machine would be composed of multifilamentary wires with mostly copper matrix, and since the B field magnitude would typically be above the penetration constant of the superconductor filaments B_p, the B field distribution throughout the armature was assumed to be the same as in a purely copper armature. For this reason, no special superconductivity packages were utilized in the FEM analysis, and the B field distributions were determined for pure copper armatures while ignoring associated thermal effects.

Second, though the armature wires experience a rotating magnetic field as opposed to a uni-axial changing field, the field changes were assumed to

be uni-axial. Prigozhin showed that rotating fields will slightly increase the current-carrying area of a superconducting wire compared to a changing B field on a single axis [15]. This will not affect our calculations beyond a slight decrease in the penetration constant B_p, so the rotating effects are ignored.

Finally, the effect of a phase shift between the applied magnetic field and the transport current is essentially ignored in our ac loss calculations. Though studies have shown that there is a dependence on the phase angle (minimum loss at 90° offset), they were all conducted at low field and current levels on HTS tapes [30]. We find that it is safest to assume the maximum loss in this situation, and if further experimental data can verify high-field dependence on phase angle then we can re-asses our loss models.

3.3.2 Procedure

Using FLUX2D, geometries were constructed for varying pole count, machine radius, and armature slot depth; these geometries were then analyzed under full-load conditions to determine the average torque in the machine and the B field distribution on an armature bar over a full electric cycle. To calculate ac loss in the entire machine, the ac loss of individual wires was computed based on the B field distribution over the armature cross section. An example distribution of B field magnitude over half of an electric cycle is shown in Fig. 3.4, illustrating the unevenness of the B field across the armature slot length. From this B field distribution, the maximum field was computed for each wire in the armature cross section, and this was doubled to determine the peak-to-peak magnetic flux swing B_m for use in the hysteresis and coupling loss equations.

With B_m known for each point in the armature cross section, the armature area can be subdivided to approximate the size and position of individual SC wires, and a B_m value can be assigned to each subdivision as if it represented a single wire. Using Eqs. 2.13 and 2.14, Q_h and Q_c can be calculated for that subdivision. Then the total SC loss in the machine armature bars can be calculated as

$$P_{ac} = \sum_i (Q_{h,i}\lambda + Q_{c,i})\pi R^2 flp \tag{3.3}$$

where $Q_{h,i}$ and $Q_{c,i}$ are the hysteresis and coupling losses in the ith super-

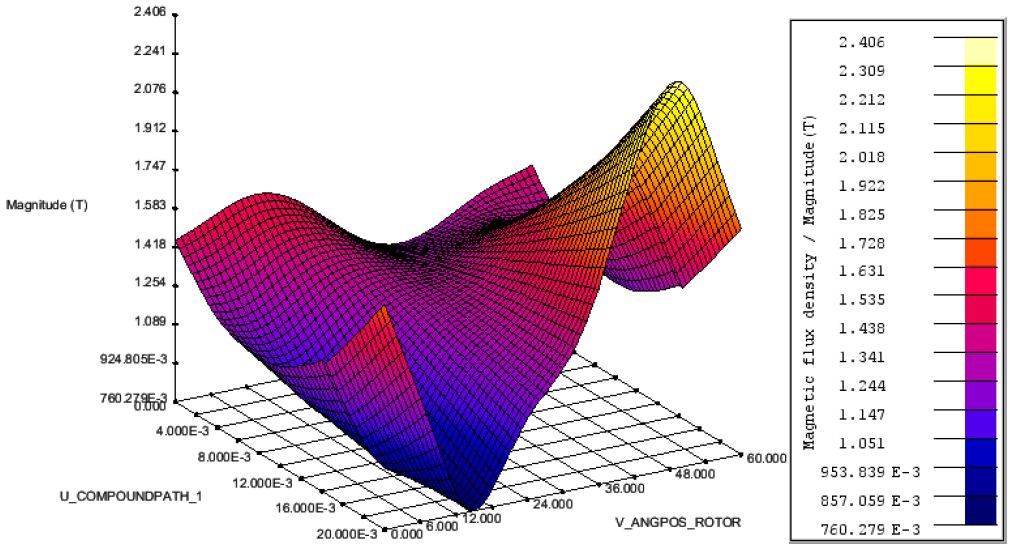

Figure 3.4: Example B field distribution across an armature bar section over an electric half-cycle.

conducting wire in the cross section of an armature bar. The summed loss Q across the armature wires is in joules per cycle per cubic meter, and needs to be multiplied by the wire cross sectional area πR^2 and frequency f to become watts per meter.[1] Finally, this quantity can be multiplied by the length l of a single turn of wire and the number of poles p to obtain the total SC loss in the armature, in watts.

In the partially SC machine geometry the armature bars are doubled, so there are six bars for each three-phase pole. However, each pole pair shares a set of armature bars, so while we would normally multiply by two to account for the extra armature bars we can also divide by two to account for the sharing between pole pairs.

With this loss quantity known for a particular machine geometry, numerous other quantities can be calculated and utilized to determine effective comparisons between various designs. These include cryogenic power requirements, machine efficiency, power density, and power density per unit of cryogenic power, and will be discussed in the following chapter.

[1]The relevant cross sectional area for hysteresis loss is in the superconducting filaments, which occupies a fraction λ of the wire cross section. This is different from coupling loss, which occurs in the entire wire cross section.

CHAPTER 4

RESULTS

4.1 Machine Parameter Variations

The machine parameters that were varied for these simulations were the slot depth and the pole count. Slot depth refers to the radial length of the armature, and pole count refers to the number of three-phase armature sets within the machine. Throughout these calculations and studies the rated power of the machine was kept constant at 10 MW.

From these initial variations in geometry, fundamental relationships between the machine design and the overall loss were determined. These relationships reduced the design space to guide more effective comparisons later on, which will be discussed in the second half of this section.

4.1.1 Geometric Relations

Fig. 4.1 shows the effect of slot depth on the superconductor loss in an 8 pole machine. This is an important relationship to determine, since electromagnetic theory would suggest that an increased slot depth will provide more torque-producing cross sectional area in the armature, thus decreasing the active length of the machine. Since superconductor loss is dependent on the total wire length, one may presume that the decrease in machine active length could nullify the additional turns of wire that result from an increased slot depth. However, Fig. 4.1 indicates otherwise, showing that a larger slot depth will lead to increased loss.

The effect of pole count on ac loss is more difficult to generalize, since the pole count has a direct effect on the radius due to the fixed geometry of the field coils in this study. Because of this, it is also useful to review the effect of pole count on other geometric parameters in the machine for a given power.

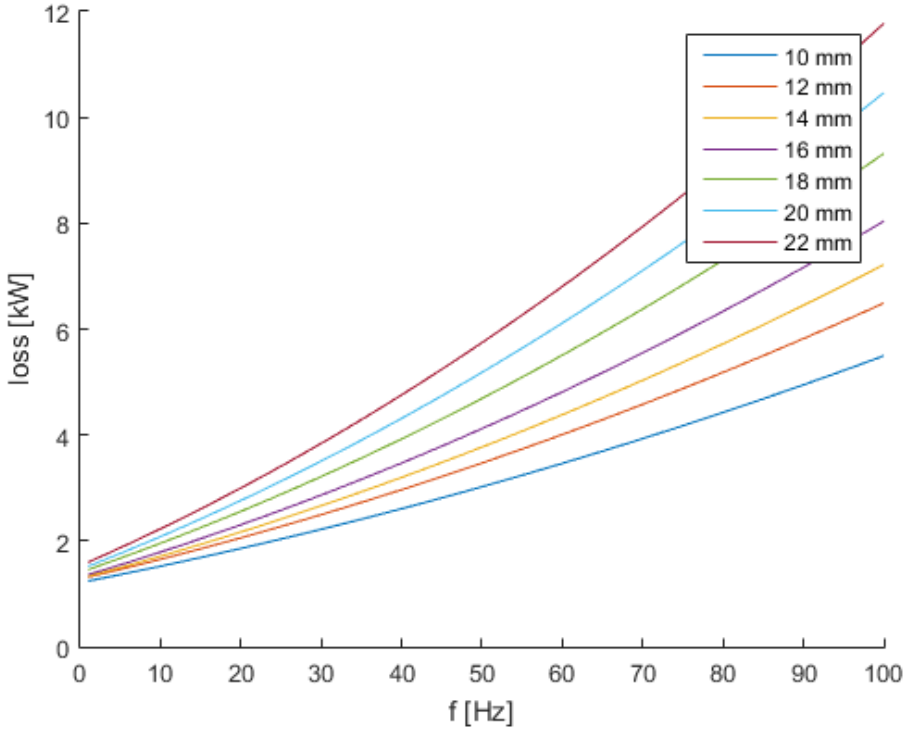

Figure 4.1: Superconductor loss for various frequencies for increased slot depth in a 10 MW, 8 pole machine

Fig. 4.2 and Fig. 4.3 show the effects of pole count on machine volume and machine length for a given slot depth. The horizontal axes of frequency and rotor speed in both figures are related as

$$n = \frac{120f}{p} \tag{4.1}$$

where n is the rotor speed in revolutions per minute (rpm), f is the frequency in Hertz and p is the number of poles. Because of this relation, any given operating frequency will not necessarily correspond to the same rotational speed for two different machines. For physics applications and initial sizing, frequency dependence is a useful metric; for machine designers and system integration engineers, however, rotor speed may be a more interesting parameter to use as a comparison baseline. For this reason, we plot relevant quantities against both frequency and speed.

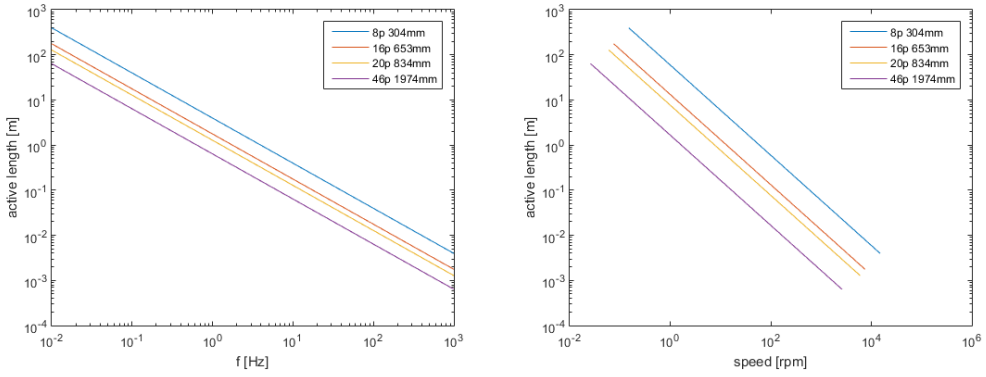

(a) (b)

Figure 4.2: Comparison of machine lengths for four values of pole count at 10 MW and 6 mm slot depth, plotted against (a) electrical frequency and (b) rotor speed.

Overall, Fig. 4.2 and Fig. 4.3 illustrate expected and well-understood relationships between operating speed and machine size for a given power. Because power is defined as torque times speed, a decrease in speed (or frequency) will require an increase in torque, and thus an increase in the machine size.

Machines with higher pole counts (directly related to machine radius in this case) will have a larger torque-producing area in their air gap and will require less active length to produce the same torque when compared to machines with few poles. However, these high pole count machines will have a larger

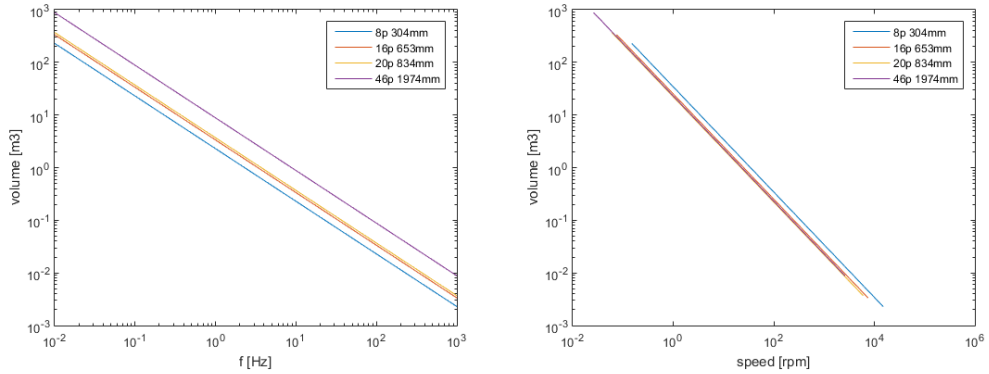

(a) (b)

Figure 4.3: Comparison of machine volume for four values of pole count at 10 MW and 6 mm slot depth, plotted against (a) electrical frequency and (b) rotor speed.

overall volume due to the square dependence of the radial cross section on the machine radius.

4.1.2 Cryogenic Power, Efficiency, and Power Density Relations

With these geometric relations, the calculated loss can be usefully compared across a wide range of designs and operating points. The first loss comparison is a simple plot of required cryogenic power to cool the machine as a function of frequency and speed, shown in Fig. 4.4.

As mentioned in Chapter 4, the total ac loss is a function of frequency, wire length, and pole count. The cryogenic power required to remove this heat is dependent on the specific power of the cryogenic system. At 20 K this can be assumed to be around 100; the amount of cryogenic power required to remove 1 W of heat load at 20 K will be 100 W. Because the cryogenics will have to cool the armature and field components of the machine, the expected loss from the dc field coils is included in this calculation. From a study on the partially superconducting machine field coils, the expected loss of each dc field coil is expected to be 1 W due to losses in the wire leads of the coils [31]. The resulting equation describing the required cryogenic power is

$$P_{cryo} = 100P_{ac} + 2p * P_{dc} \tag{4.2}$$

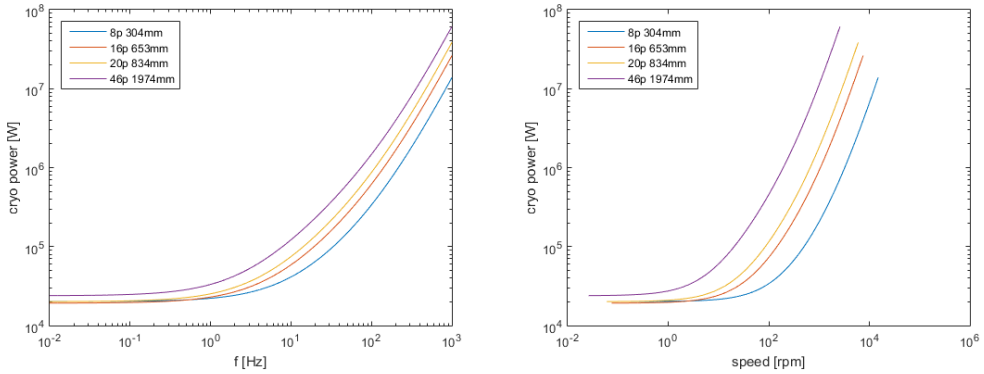

(a) (b)

Figure 4.4: Comparison of cryogenic power for four values of pole count at 10 MW and 6 mm slot depth, plotted against (a) electrical frequency and (b) rotor speed.

where P_{dc} is the loss in each dc coil, multiplied by 2 to account for both main and compensating coils and p to account for the number of poles.

Fig. 4.4 illustrates the dependence of ac loss on frequency, with a constant low value for sub-hertz frequencies. In this low frequency range, the resulting cryogenic power is extremely low while the required length of the machine is extremeley high. The two cancel out, leaving a constant loss. As the frequency increases, superconducting ac effects start to compound the loss, as expected. A comparison with speed indicates that larger machines with higher pole counts are likely not suitable for high speed applications due to the increased loss and cryogenic power requirements at lower speeds.

Determination of the cryogenic loss directly leads to the machine efficiency η, which can be calculated as

$$\eta = \frac{P_{rated}}{P_{rated} + P_{cryo}} \tag{4.3}$$

where P_{rated} is the SC machine's rated power, in this case 10 MW. Values of η closer to 1 indicate a more efficient machine. In Fig. 4.5, the efficiency of the machine is plotted for each analyzed pole count, and again we see that larger machines are confined to a lower range of operating speeds due to their lower relative efficiency.

While loss and efficiency are useful metrics for measuring the performance and operating range of an electric machine, they do not address the initial goal of the machine's design, which is to have high power and low weight.

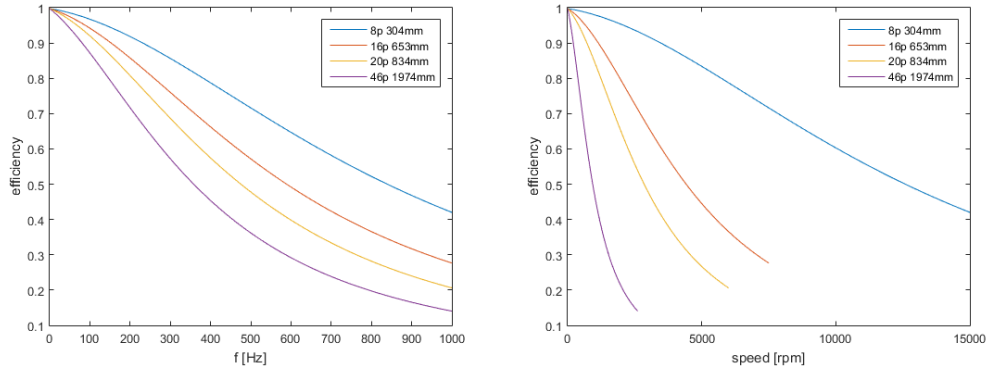

(a) (b)

Figure 4.5: Comparison of efficiency for four values of pole count at 10 MW and 6 mm slot depth, plotted against (a) electrical frequency and (b) rotor speed.

This metric is known as specific power, and is a well-known parameter for machine comparisons. Unfortunately, the determination of specific power requires intimate knowledge of the mechanical construction of the machine, which is not entirely available at this stage of the design. For this reason, the power density (power per unit volume) is used instead to compare the various designs.

Fig. 4.6 shows the power density of the various designs, which is not affected by the ac loss in the system. This is purely based on the geometry and operating point of the design, and we have already shown a similar plot for volume in Fig. 4.3.

A more interesting metric is the ratio of the power density to the amount of required cryogenic power, which we will call Power Density to Cryo (PDC). This encompasses the tradeoff between power density and loss, as increased power density is associated with increased speed, a parameter that is itself associated with increased loss. In the logarithmic plots, power density appears linear relative to the exponential shape of the cryogenic power. As a result, the PDC ratio should have an absolute maximum point representing the most desirable operating point to balance power density and ac losses.

Fig. 4.7 shows the PDC plots for each pole count. The smaller machines have maximum points at a higher speed, with a larger ratio of power density to cryogenic power compared to the higher-pole-count machines. The maximum points occur around 700 rpm (45 Hz) for the 8 pole design, 250 rpm

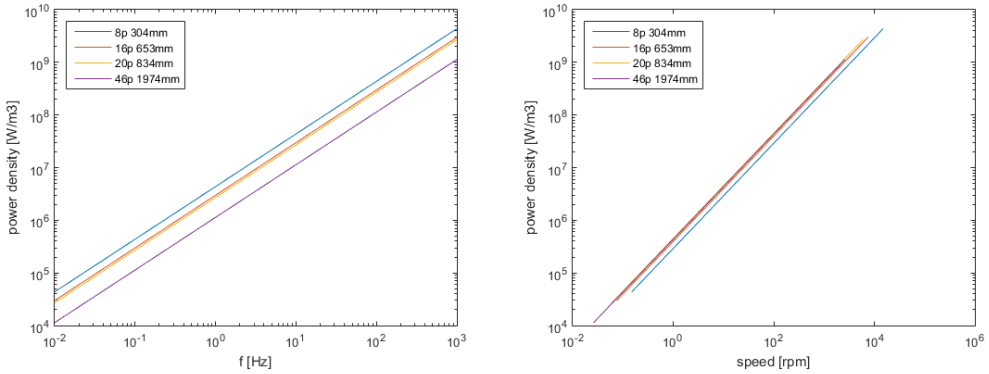

(a) (b)

Figure 4.6: Comparison of power density for four values of pole count at 10 MW and 6 mm slot depth, plotted against (a) electrical frequency and (b) rotor speed.

(30 Hz) for the 16 pole design, 125 rpm (20 Hz) for the 20 pole design, and 45 rpm (18 Hz) for the 46 pole design.

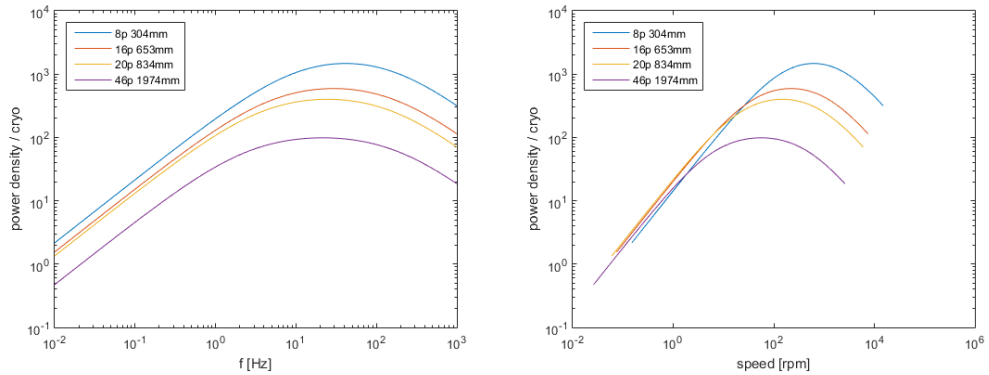

(a) (b)

Figure 4.7: PDC for four values of pole count at 10 MW and 6 mm slot depth, plotted against (a) electrical frequency and (b) rotor speed.

Now it is useful to venture back to the initial slot depth variations and see how that parameter affects the PDC. At the beginning of this chapter, an initial investigation indicated that loss would increase with slot depth, suggesting a small slot depth in the design. However, the volume and power density were not examined as functions of slot depth, and that information can be expressed (including loss) in the PDC.

The variation in PDC with slot depth is shown as maximum points in Fig. 4.8. A zoomed-in version can be seen in Fig 4.9 with a clearer shape and a

peak optimum point at 10 mm slot depth.

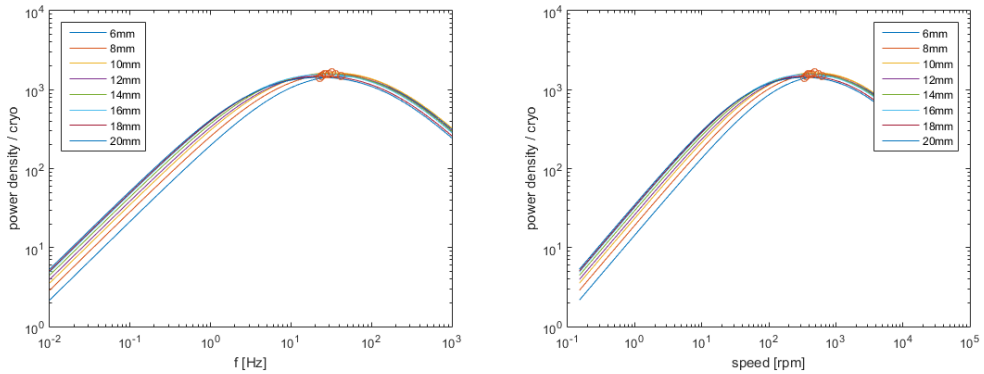

(a) (b)

Figure 4.8: PDC maxima for an 8 pole design at 10 MW and varying slot depth, plotted against (a) electrical frequency and (b) rotor speed.

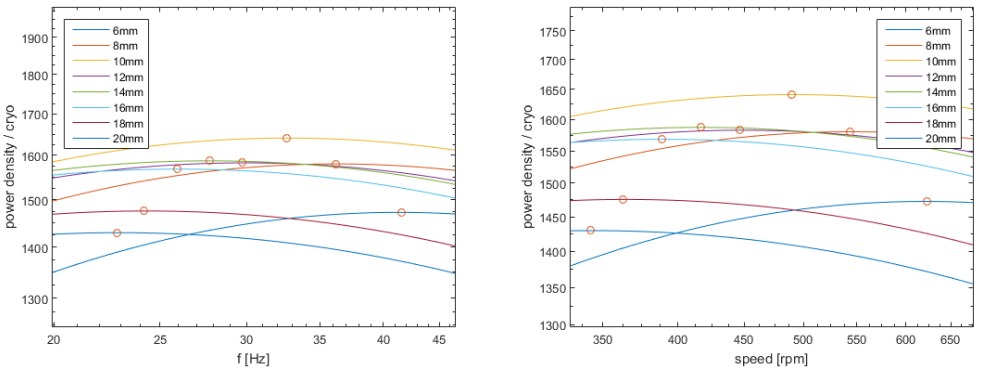

(a) (b)

Figure 4.9: Zoom view of PDC maxima for an 8 pole design at 10 MW and varying slot depth, plotted against (a) electrical frequency and (b) rotor speed.

4.2 Comparison with Partial SC Design

From these relations and plots, an initial optimized design was chosen for two machine sizes. It should be noted that these designs are merely considered optimal within the range of the examined parameters, yet they can still serve as useful metrics for comparison with existing designs. One such comparison

is shown in Table 4.1, where two fully SC designs are compared with existing partial SC designs from prior work.

Table 4.1: Comparison of partial and fully SC design parameters and results

Parameter	Units	Fully SC Design 1	Partial SC Design 1	Fully SC Design 2	Partial SC Design 2
Pole count		8	46	8	46
Speed	[rpm]	8000	10	8000	10
Slot depth	[mm]	10	25.4	10	100
Active length	[m]	0.0074	0.157	0.155	1.25
Volume	[m^3]	0.0043	0.088	2.0	19.75
Power density	[MW/m^3]	2300	110	4.6	0.5
Cryo power	[kW]	4480	16	58	92
Efficiency	[%]	69.0	99.8	99.4	99.0
PDC		522	7080	79	5.6

In the 8 pole designs, the partial SC machine operates with less loss at a higher volume; however, its cooling requirements far outweigh any volume benefits that the fully SC design offers. Such a large cooling requirement drastically affects the overall performance of the machine, evidenced in the low efficiency and relative PDC in the fully SC machine. From this, and given current state of the art SC wire, a partially superconducting machine is still more viable than a fully superconducting one for high speeds and frequencies.

The 46 pole designs show the opposite, however. In this case the partially SC machine requires much more volume and, surprisingly, more cooling. This is due to the superconducting dc field coils, which contribute significant loss when multiplied by the high pole count. As discussed previously, though superconductors themselves have no dc loss, superconducting wires will have some small loss especially in the power connections. This loss is also more significant in the partial SC design due to the higher specific power required to cool at 4 K versus 20 K. From this comparison, we can conclude that a fully superconducting machine is indeed viable for a large, slow moving machine in perhaps a wind power application.

Fig 4.10 shows the two partial SC design points plotted over the PDC curves. As a general rule, a design point would need to be below the PDC curve to be considered less viable than the fully SC machine option in terms

of power density and loss. Since the 8 pole partial SC design is above the 8 pole curve, it is not feasible to construct a comparative 8 pole fully SC design. Likewise, since the 46 pole partial SC design is far below the 46 pole curve, it is certainly feasible to investigate larger fully SC machines.

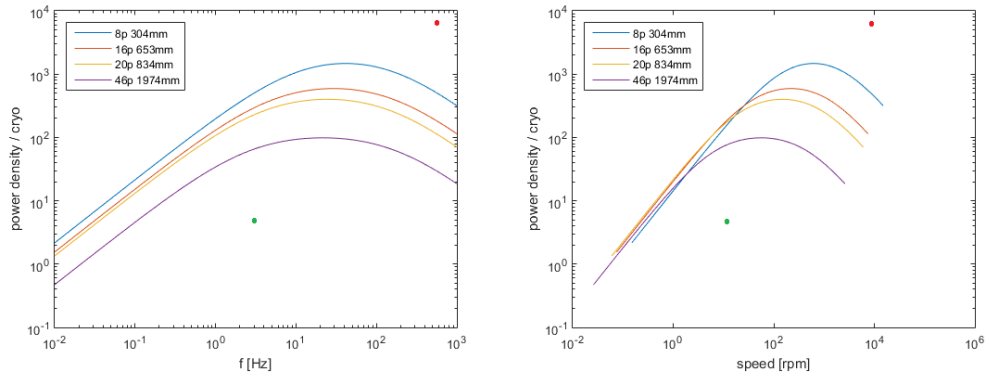

(a) (b)

Figure 4.10: PDC plots for four pole values at 10 MW and 6 mm slot depth, plotted against (a) electrical frequency and (b) rotor speed. The dots indicate relative performance of partial SC 8 pole (red) and 46 pole (green) designs.

4.2.1 Assumptions and Limitations

It is worthwhile to consider the limitations of the loss model as well as the physical implications of the results before concluding this work. First, the physical limits of the results should be addressed. In the figures above, volume and active length were shown to decrease with increased speed, sometimes to unrealistically small values. For example, a machine active length of 7 mm for the 8 pole, 8000 rpm case would not be practical as armature ends would dominate the torque as well as set a lower bound on the length and volume. Additionally, many superconductor manufacturers are limited in the quantity of wire that they can produce in a given time period, and some SC wire is performance limited based on length. As a result, many of the lower frequency and long active length designs may be unviable from a production or performance standpoint. This reasonably leaves the 1-100 Hz range as an area of practical confidence.

An additional consideration should be given to the metric of PDC, or the

'Power Density to Cryo' ratio. This uses the volumetric power density as a measuring tool, which can be useful in theory but not necessarily in practice. A more useful parameter among systems integration engineers is the specific power (power per unit weight), which is difficult to determine in a sizing study such as this one due to an incomplete mechanical model of the system. However, one can presume that the plot of specific power versus frequency will have a similar shape to that of the power density, so the two can be considered analogous at the first order. With another level of interpretation, one can surmise that the slope of the plot of specific power will likely decrease over the frequency range as more cryocoolers are required to offset the heat load, so the PDC (or equivalent ratio using specific power) maximum would shift to the left. This will not impact the comparison between partial and fully SC machines too much, as the chosen design points are far above and below their respective PDC lines.

A major assumption of this study is that the established loss models, which are primarily validated with experiments at low field amplitudes, will accurately predict results at high fields. There is reasonable evidence to suggest that large fields exhibit predictable behavior above the penetration field level B_p, but actual data is scarce for such operation. A large part of this is due to the difficulty in producing and operating a strong sinusoidal magnetic field for testing purposes. One option is to measure the loss due to strong pulsed fields and extend that to relate periodic waveforms, but that has not been attempted to the author's knowledge.

Finally, mechanical considerations were entirely ignored in this work. These considerations include implementation for cooling, analysis of torque and shear stress, and models for the rotating forces and compressive strain within the SC wires. A reasonable cooling system would require one or more cryocoolers, a liquid refrigerant loop, pressure release mechanisms, vacuum vessels, quench protection, rotating mechanical coupling for the rotor, and more. Analysis of the rotor torque would require the implementation of more mechanical details in the rotor such as material type, material thickness, and leakage heat paths. Finally the forces acting on the SC wire in the armature will affect their strain, which is one of the four parameters that can lead to loss of superconductivity. A detailed analysis of compressive and tensile strain resulting from rotating forces and electromagnetic Lorentz forces would be required to retire that area of risk. Overall, there is much work to

be done to validate the mechanical uncertainties of these designs, but this can be done later.

CHAPTER 5

CONCLUSIONS AND FUTURE WORK

In this work, a study was performed to analyze the feasibility of a design change from a partially superconducting machine to a fully superconducting one. Due to large ac losses and expensive superconducting wire, fully SC machines have not seen much popularity, and partial SC designs are employed instead. However, with projected and demonstrated improvements in superconductor and cryogenic technology, the fully SC dream comes closer to reality each year.

From the results of this study, it is clear that the state of the art of SC wire is at a point where it can be feasibly employed in a fully SC machine design for low frequency applications such as wind power, but not in high-speed, high frequency applications such as aircraft propulsion. While the goal is to operate a machine at higher speed for aircraft, superconductor losses are simply too large for the desired speed range. There is some intermediate fully SC machine sizing that can operate at a higher speed with a higher power density than partial SC, but that exact point is unknown from this study. The shapes of the power density plots suggest these speeds may occur around 200-500 rpm, which is useful for applications such as ship propulsion or some form of low-speed hydro-electric generation.

While our conclusions may be useful at a high level, there is still much work to be done to strengthen our confidence in the results while also refining the model. In terms of electromagnetic analysis, there is substantial room for optimization within the machine design for designs utilizing new pole counts and radii. These optimizations can improve upon armature slot size, dc coil geometry and electric loading. With the existing loss models, more geometries can be analyzed as partial/fully SC machines and plotted against the existing PDC lines. The current two points of comparison can then be connected with more data, and the crossover point between partial and fully SC machine feasibility can be determined.

An FEM simulation for superconducting ac loss was unavailable due to software license restrictions, though this would certainly help validate some of the theoretical hysteresis losses in the superconducting wire.

Mechanically, there is much to validate structurally and thermally, but this may be better as a design step after the electromagnetic sizing is complete. It is by no means insignificant, however, as increased torque load and cooling difficulty pose great challenges in superconducting machine design.

Though more analysis can help, there is no substitute for experimental data. As such, loss experiments on superconducting wire samples in machine-like conditions would be very useful in more confidently validating the models that were used in this study. Such experiments would include measurement of ac loss due to simultaneous high-field and low current scenarios; to the author's knowledge, there is no data for superconductor loss in MgB_2 due to alternating magnetic fields above 1T, with or without ac transport current. Additionally, an experimental comparison of rotating magnetic field loss and uniaxial magnetic field loss above penetration levels on circular wire would help establish a clearer relationship between the losses due to the two types of applied magnetic field.

REFERENCES

[1] M. Bradley and C. Droney, "Subsonic ultra green aircraft research: Phase II - Volume II - Hybrid electric design exploration," NASA, Tech. Rep., 2015.

[2] H. D. Kim, "Distributed propulsion vehicles," in *Congress of the Aeronautical Sciences*, 2010.

[3] Intergovernmental Panel on Climate Change, "Aviation and the global atmosphere. A special report of IPCC working groups I and III." Tech. Rep., 1999. [Online]. Available: http://www.ipcc.ch/ipccreports/sres/aviation/

[4] International Air Transport Association, "Vision 2050," Tech. Rep., 2011.

[5] X. Zhang and K. S. Haran, "High-specific-power electric machines for electrified transportation applications-technology options," in *2016 IEEE Energy Conversion Congress and Exposition (ECCE)*, Sept 2016, pp. 1–8.

[6] B. Gamble, G. Snitchler, and T. Macdonald, "Full power test of a 36.5 MW HTS propulsion motor," *IEEE Transactions on Applied Superconductivity*, vol. 21, no. 3 PART 2, pp. 1083–1088, 2011.

[7] H. Kamerlingh Onnes, "Further experiments with liquid helium," *Leiden Communications*, vol. 120b, 122b, pp. 261–271, 1911.

[8] M. Tinkham, *Introduction to Superconductivity: Second Edition*, ser. Dover Books on Physics. Dover Publications, 2004. [Online]. Available: https://books.google.com/books?id=k6AO9nRYbioC

[9] G. S. Withers and J. R. Toggweiler, "Superconductivity above 130 K in the Hg-Ba-Ca-Cu-O system," *Nature*, vol. 363, pp. 56–58, 1993.

[10] A. Leggett, "PHYS 598SC1 Lecture Notes," 2015. [Online]. Available: https://courses.physics.illinois.edu/phys598sc1/

[11] N. Mitchell, D. Bessette, K. Okuno, H. Takigami, E. Zapretilina, and P. Bruzzone, "Magnet superconducting and electrical design criteria," ITER, Tech. Rep.

[12] J. W. Ekin, "Four-dimensional J-B-T-ϵ critical surface for superconductors," *Journal of Applied Physics*, vol. 54, no. 1, pp. 303–306, 1983.

[13] C. P. Bean, "Magnetization of hard superconductors," *Phys. Rev. Lett.*, vol. 8, no. 6, pp. 250–253, Mar 1962. [Online]. Available: http://link.aps.org/doi/10.1103/PhysRevLett.8.250

[14] F. Grilli, E. Pardo, A. Stenvall, and D. N. Nguyen, "Computation of losses in HTS under the action of varying magnetic fields and currents," *IEEE Transactions on Applied Superconductivity*, vol. 24, no. 1, 2014.

[15] L. Prigozhin, "The bean model in superconductivity: Variational formulation and numerical solution," *Journal of Computational Physics*, vol. 200, pp. 190–200, 1996.

[16] M. Wilson, *Superconducting Magnets*. Clarendon Press Oxford, 1983.

[17] W. T. Norris, "Calculation of hysteresis losses in hard superconductors carrying ac: isolated conductors and edges of thin sheets," *Journal of Physics D: Applied Physics*, vol. 3, no. 4, pp. 489–507, 1970.

[18] W. Carr, "Ac loss from the combined action of transport current and applied field," *IEEE Transactions on Magnetics*, vol. 15, no. 1, pp. 240–243, Jan 1979.

[19] J. J. Rabbers, D. C. van der Laan, B. ten Haken, and H. H. J. ten Kate, "Magnetisation and transport current loss of a BSCCO/Ag tape in an external ac magnetic field carrying an ac transport current," *IEEE Transactions on Applied Superconductivity*, vol. 9, no. 2, pp. 1185–1188, June 1999.

[20] S. S. Kalsi, "Superconducting wind turbine generator employing MgB2 windings both on rotor and stator," *IEEE Transactions on Applied Superconductivity*, vol. 24, no. 1, pp. 47–53, 2014. [Online]. Available: http://ieeexplore.ieee.org/lpdocs/epic03/wrapper.htm?arnumber=6670049

[21] G. Snitchler, B. Gamble, and S. S. Kalsi, "The performance of a 5 MW high temperature superconductor ship propulsion motor," *IEEE Transactions on Applied Superconductivity*, vol. 15, no. 2 PART II, pp. 2206–2209, 2005.

[22] R. Alhasan, T. Lubin, Z. M. Adilov, and J. Lévêque, "A new kind of superconducting machine," *IEEE Transactions on Applied Superconductivity*, vol. 26, no. 3, pp. 1–4, 2016.

[23] H. J. Sung, G. H. Kim, K. Kim, S. J. Jung, M. Park, I. K. Yu, Y. G. Kim, H. Lee, and A. R. Kim, "Practical design of a 10 MW superconducting wind power generator considering weight issue," *IEEE Transactions on Applied Superconductivity*, vol. 23, no. 3, pp. 0–4, 2013.

[24] K. S. Haran, D. Loder, T. O. Deppen, and L. Zheng, "Actively shielded high-field air-core superconducting machines," *IEEE Transactions on Applied Superconductivity*, vol. 26, no. 2, pp. 98–105, March 2016.

[25] M. Gouge, J. Demko, B. McConnell, and O. J. M. Pfotenhauer, "Cryogenics assessment report," Oak Ridge National Laboratory USA, Tech. Rep., 2002. [Online]. Available: http://ornl.org/sci/engineering_science_technology/cooling_heating_power/htsc/documents/pdf/CryoAssessRpt.pdf

[26] K. Haran, S. Kalsi, T. Arndt, H. Karmaker, R. Badcock, B. Buckley, T. Haugan, M. Izumi, D. Loder, J. Bray, and P. Masson, "Superconducting rotating machines - development status and technology roadmap," *Superconductor Science and Technology*, in process 2017.

[27] F. Wan, M. D. Sumption, M. A. Rindfleisch, M. J. Tomsic, E. W. Collings, and A. Samples, "Architecture and transport properties of multifilamentary MgB2 strands for MRI and low ac loss applications," *IEEE Transactions on Applied Superconductivity*, vol. 27, no. 4, pp. 1–5, 2017.

[28] G. Li, J. B. Zwayer, C. J. Kovacs, M. A. Susner, M. D. Sumption, M. A. Rindfleisch, C. J. Thong, M. Tomsic, and E. W. Collings, "Transport critical current densities and n -values of multifilamentary MgB2 wires at various temperatures and magnetic fields," *IEEE Transactions on Applied Superconductivity*, vol. 24, no. 3, pp. 1–5, 2014.

[29] C. Y. Ho, M. W. Ackerman, K. Y. Wu, T. N. Havill, R. H. Bogaard, R. A. Matula, S. G. Oh, and H. M. James, "Electrical resistivity of ten selected binary alloy systems," *Journal of Physical and Chemical Reference Data*, vol. 12, no. 2, pp. 183–322, 1983.

[30] S. Ashworth and M. Suenaga, "Measurement of ac losses in superconductors due to ac transport currents in applied ac magnetic fields," *Physica C: Superconductivity*, vol. 313, no. 34, pp. 175 – 187, 1999.

[31] D. Loder, M. Feddersen, R. Sanchez, K. Haran, M. Sumption, C. Kovacs, M. Majoros, E. W. Collings, D. Doll, X. Peng, and J. Yue, "Demonstration of a practical Nb_3Sn coil for an actively shielded generator," *IEEE Transactions on Applied Superconductivity*, vol. 27, no. 4, pp. 1–7, June 2017.